

Street canyon ventilation: Combined effect of crosssection geometry and wall heating

*Original*

Street canyon ventilation: Combined effect of crosssection geometry and wall heating / Fellini, Sofia; Ridolfi, Luca; Salizzoni, Pietro. - In: QUARTERLY JOURNAL OF THE ROYAL METEOROLOGICAL SOCIETY. - ISSN 0035-9009. - ELETTRONICO. - (2020). [10.1002/qj.3795]

*Availability:*

This version is available at: 11583/2818092 since: 2020-04-29T19:39:42Z

*Publisher:*

Wiley-Blackwell on behalf of the Royal Meteorological Society

*Published*

DOI:10.1002/qj.3795

*Terms of use:*

This article is made available under terms and conditions as specified in the corresponding bibliographic description in the repository

*Publisher copyright*

Wiley preprint/submitted version

This is the pre-peer reviewed version of the [above quoted article], which has been published in final form at <http://dx.doi.org/10.1002/qj.3795>. This article may be used for non-commercial purposes in accordance with Wiley Terms and Conditions for Use of Self-Archived Versions..

(Article begins on next page)

# Street canyon ventilation: combined effect of cross-section geometry and wall heating

Sofia Fellini<sup>1,2</sup> | Luca Ridolfi<sup>2</sup> | Pietro Salizzoni<sup>1</sup>

<sup>1</sup>Laboratoire de Mécanique des Fluides et d'Acoustique, UMR CNRS 5509, Université de Lyon, Ecole Centrale de Lyon, INSA Lyon, Université Claude Bernard Lyon I, Ecully, France

<sup>2</sup>Department of Environmental, Land, and Infrastructure Engineering, Politecnico di Torino, Turin, Italy

Correspondence

Sofia Fellini, Department of Environmental, Land, and Infrastructure Engineering, Politecnico di Torino, Turin, Italy  
Email: sofia.fellini@polito.it

Funding information

Understanding the dynamics of mass exchange between a street canyon and the overlying atmosphere is crucial to predict air quality in urban areas. Despite the large number of studies on this topic, there are many aspects that still need to be clarified. Among these, one is certainly the role of thermal stratification in street canyon ventilation. In order to fill this gap, this study evaluates how the combined effect of street canyon geometry, wall roughness and differential heating of the building façades influences pollutant dispersion within the canyon and out of it. The study was carried out in a wind tunnel, adopting an idealized urban geometry made-up of square bars placed normal to the wind direction. The boundary conditions inside the canyon were modified by heating its windward and leeward walls, by changing its aspect ratio and by introducing roughness elements at walls. A passive scalar was injected from a line source at ground level. The flow and concentration fields were measured in a cross-section of the canyon. Characteristic exchange velocities within the canyon and towards the external flow were estimated comparing the experimental data with an analytical model for the cavity wash-out. Results show that the transition from one recirculating cell to two counter-rotating cells inhibits canyon ventilation, with a consequent increase in pollutant concentration at the pedestrian level. This transition occurs as the

cavity aspect ratio increases and is facilitated by adding roughness elements at the windward wall. Heating the leeward wall has negligible effects on canyon ventilation. Heating the windward wall accelerates pollutant removals in square cavities, while it contributes to a worsening of air quality in narrow cavities. Finally, the wash-out times of the cavity are discussed in terms of a relative contribution of the mean advective motion and its turbulent counterpart.

#### KEY WORDS

Street canyon, Urban air pollution, Turbulent transfer of passive scalars, Wind-tunnel experiments, Thermal effects, Solar radiation

## 1 | INTRODUCTION

2 In 2050, more than 70% of the world population will live in urban areas [23]. Despite recent efforts in  
3 environmental policies, air pollution in cities still represents the biggest environmental risk to health [78]. In  
4 particular, citizens in developing countries are the most impacted by poor air quality.

5 To address this rapid urbanization, solutions for more sustainable cities are extensively sought [e.g., 21,  
6 10, 9]. The assessment and implementation of these mitigation strategies require a deep understanding of the  
7 urban microclimate [65, 57, 22] which is the result of the complex interaction between physical phenomena  
8 (e.g., wind, atmospheric stability, solar radiation) and the city (e.g., buildings, anthropogenic emissions, urban  
9 vegetation).

10 In this framework, the prediction of pollutant transfer within and above a street canyon is crucial to develop  
11 urban dispersion models for operational purposes [80, 74, 75, 72, 18]. The street canyon is the fundamental  
12 unit of the urban geometry. It is composed by a narrow street flanked by buildings on both sides, creating  
13 a canyon-like environment. In street canyons, the concentration of pollutants is high due to the presence of  
14 (ground level) vehicular and anthropogenic emissions and to the weak air ventilation caused by a recirculating  
15 motion between the buildings. The close proximity between emitters (vehicles, chimneys) and receptors makes  
16 these regions extremely vulnerable to health risks [24]. Generally, the maximum concentration occurs when  
17 the wind blows perpendicular to the street canyon, inducing a recirculating flow that confines the transport  
18 of pollutants. Another critical case is represented by very long streets, in which pollutant accumulation, due  
19 to the longitudinal wind, is responsible for concentrations close to or even higher than those observed with a  
20 wind direction perpendicular to the street axis [73].

21 While horizontal advection at the lateral ends of a street canyon is the dominant ventilation mechanism  
22 for longitudinal and oblique wind directions [e.g., 12], when the wind is perpendicular to the street, the air  
23 quality mainly depends on the vertical pollutant exchange with the atmosphere above roof-level. Several  
24 studies focused on the influence of different dynamical and geometrical parameters on this vertical transfer.  
25 Considering the problem as two-dimensional, the flow dynamics are analysed in a generic cross-section of

26 the canyon, i.e. in a two-dimensional cavity. The effect of the cavity geometry on the flow dynamics within  
27 the canyon has become a classical case-study in fluid mechanics. A number of works [27, 56, 30, 4] has  
28 demonstrated that the formation of secondary vortices in narrow cavities inhibits the canyon ventilation. The  
29 studies of Murena and Mele [49] and Llaguno-Munitxa et al. [42] evidenced the role of roughness elements (e.g.,  
30 balconies) on the building walls in reducing the pollutant transfer from the street to the above atmosphere.  
31 In addition to the influence of large and small geometrical scales, the efficiency of street canyon ventilation  
32 has been investigated with respect to several other aspects. Among these, we cite here the experiments of  
33 Salizzoni et al. [63, 62], who investigated the role of the external turbulence, Solazzo et al. [70], who performed  
34 numerical simulations about the effect of traffic induced turbulence on dispersion processes within the street,  
35 and Gromke and Ruck [20], who tried to clarify the impact of trees on the canyon ventilation.

36 Besides the analysis of these dynamical mechanisms, a growing interest has been devoted to the study  
37 of buoyancy effects on the air flow within the canyon. Thermal fluxes generate buoyancy forces that have a  
38 relevant influence especially in low wind condition. These effects are primarily associated to solar radiation  
39 which induces temperature differences between the canyon walls of about 15 K at mid latitudes [43, 55]. A  
40 deep understanding of the interaction between wind and buoyancy forces within the streets is crucial for the  
41 implementation of natural or hybrid ventilation techniques [26, 19], for the improvement of energy performance  
42 in buildings [65], and for mitigating the heat island effect through in-canyon vegetation [2, 36] and urban  
43 planning [76].

44 Variations in the flow streamlines within a street canyon due to heat fluxes at the canyon walls and bottom  
45 were investigated numerically by the RANS models of Sini et al. [67] and Kim and Baik [32]. Sini et al. [67]  
46 found that when a wind is blowing perpendicular to the canyon and the downstream wall is heated, two  
47 counter-rotating vortices are formed. The CFD simulations of Xie et al. [79] confirmed these findings but  
48 observed that these secondary structures were overestimated with respect to the wind-tunnel observations of  
49 Kovar-Panskus et al. [33]. Solazzo and Britter [69] simulated weak buoyancy effects in the canyon to estimate  
50 a typical vertical exchange velocity. More recently, the LES studies of Cai [11] and Li et al. [39, 38] provided  
51 insights into the turbulence structure within a heated canyon, while Nazarian et al. [51] investigated the  
52 effect of three dimensional surface heating. With numerical simulations, a great variety of scenarios can be  
53 analysed. However, these simulations are very sensitive to the domain size [16], to the sub-grid model and to  
54 the treatment of the boundary conditions.

55 Field studies on the effect of thermal fluxes in street canyons were conducted in different European and  
56 Asian cities [50, 43, 55, 52]. In these studies, the influence of thermal fluxes seemed to be limited to a thin  
57 layer close to the heated wall, and the occurrence of secondary recirculating structures was not detected.

58 Few wind-tunnel experiments were performed to investigate the role of wall heating on the flow structure  
59 within a street canyon. This is mainly due to practical difficulties in complying with the similarity criteria  
60 for the internal Froude number, i.e. the dimensionless number expressing the ratio of inertial to buoyancy  
61 forces (see Section 2.3). In fact, very large temperature differences within the canyon are required to reproduce  
62 realistic buoyancy conditions in wind tunnel models with high scaled street canyons. Uehara et al. [77] analysed  
63 the effects of atmospheric stability on the the flow within a street canyon heating the floor of the wind tunnel.  
64 Kovar-Panskus et al. [33] proposed a wind-tunnel experiment with the direction of the wind normal to the  
65 canyon and a differential heating of the cavity walls. In the experiment, the downstream wall of a square  
66 canyon was heated and four external velocities were applied in order to generate different buoyancy conditions.  
67 They observed the formation of a stagnant flow at the bottom of the cavity, as the Froude number decreases.  
68 By means of PIV (Particle Image Velocimetry) measurements, Allegrini et al. [3] investigated the flow field in

69 a square cavity for a wider range of configurations: heating of the (i) upstream wall, (ii) downstream wall, (iii)  
70 canyon ground, and (iv) all three surfaces together. The formation of a second counter-rotating vortex was  
71 evident for the configuration with the heating of the windward wall. In all cases, an increase in the turbulent  
72 kinetic energy inside the cavity was measured. Similar results for the flow field were found by Marucci and  
73 Carpentieri [44], who in addition analysed the effect of stratification in the approaching flow. By the release  
74 of a tracer from a ground level source, dispersion measurements were also performed.

75 Besides these recent works, the shortage of laboratory experiments represents a significant limitation for  
76 the validation of the widespread numerical studies. To date, we observe the lack of a comprehensive analysis  
77 of the combined effect of the street canyon geometry and the buoyancy conditions within it. These factors  
78 proved to be key in determining the fluid dynamical conditions in the street canyon.

79 In this picture, the goal of this study is to evaluate, by means of wind-tunnel experiments, how different  
80 geometry and heat conditions within a two-dimensional street canyon determine the flow and the dispersion of  
81 a passive scalar within the cavity itself. To this aim, the flow field for an airflow perpendicular to the canyon  
82 is analysed for eight different aspect ratios of the cavity in isothermal conditions. The effect of roughness  
83 elements on the canyon walls is also investigated for these configurations. For a square and a narrow cavity,  
84 thermal effects are examined. The upwind and downwind walls are alternatively heated and different thermal  
85 fluxes are experimented. The spatial coherence of the turbulent field is investigated by means of PIV. Steady  
86 and unsteady measurements of concentration are performed in the cavity with a Flame Ionisation Detector  
87 (FID) system, in order to investigate both the spatial distribution and the temporal evolution of pollutants  
88 released at the ground level.

89 The variety of experimental configurations, the different measured quantities and their analysis sheds  
90 light on the fluid-dynamical mechanisms that govern the wash-out of a two-dimensional street canyon for a  
91 perpendicular wind direction. This is done to improve the modelling of air pollution and heat transfer in  
92 cities.

## 93 2 | METHODOLOGY

### 94 2.1 | Experimental setup

95 The experiments were performed in a closed-circuit wind tunnel (Figure 1) at the laboratory LMFA (Labora-  
96 toire de Mécanique des Fluides et d'Acoustique) at the École Centrale de Lyon. The test section of this tunnel  
97 is 8 m long, 1 m high and 0.7 m wide. Irwin spires [29] with a height of 0.4 m were placed at the entrance of the  
98 test section. A total of 65 aluminium bars were arranged normal to the wind direction, along the entire length  
99 of the wooden floor of the wind tunnel. The bars were of section 0.06 m x 0.06 m, with a length ( $L$ ) of 0.7 m  
100 extending over the entire width of the tunnel, and with a spacing of 0.06 m between them. In this way, we  
101 obtained a regular set of parallel street canyons with a constant aspect ratio of one, with the exception of the  
102 canyon where the measurements were taken which had a variable aspect ratio. This canyon was located 5 m  
103 downstream of the vortex generators, i.e. downwind of an urban canopy of about 40 canyons. In this way, the  
104 fully development of the approaching flow was guaranteed [46, 59] and a neutral atmospheric boundary layer  
105 with depth  $\delta = 0.6$  m was obtained. The blockage ratio of the model to the cross-section of the wind tunnel  
106 was 6%. Before starting the experiments, we ensured that the incident velocity field was two-dimensional by  
107 measuring velocity profiles upstream and downstream of the canyon at different transversal positions. These  
108 velocity profiles confirmed that the flow field was uniform in the transverse direction, with variations of less

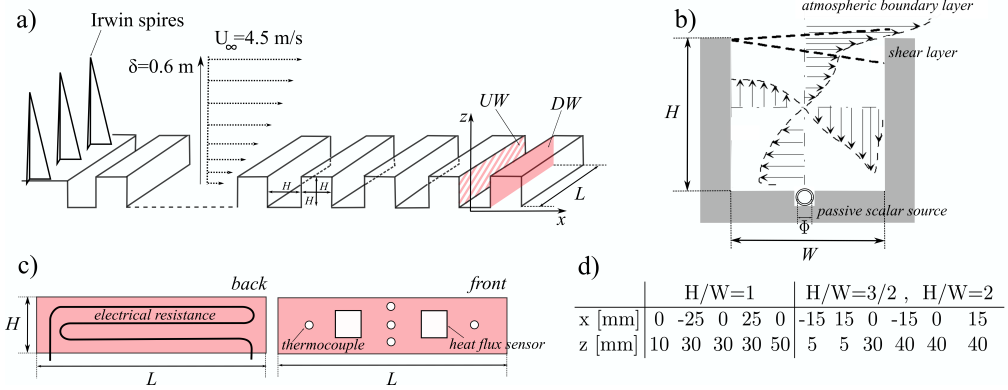


FIGURE 1 a) Overview of the wind tunnel installation with the position of the street canyon. b) Sketch of the canyon cross-section with the qualitative representation of the two-dimensional flow. The line source is located in a slot cut in the tunnel floor. c) Sketch of the set-up for the configurations with heating of the downwind wall (DW). d) Horizontal ( $X$ ) and vertical ( $Z$ ) coordinates of the points where the wash-out curves were measured.

109 than 1% for the mean flow and 5% for the turbulence quantities. Moreover, concentration measurements were  
 110 performed along the longitudinal axis of the canyon at various heights (with the linear source of tracer placed  
 111 at ground level) demonstrating the two-dimensional nature of the mean concentration field within the canyon.

112 The height ( $H$ ) of the canyon in which the measurements were performed was 0.06 m (i.e. one tenth of  
 113 the boundary layer height), while its width ( $W$ ) varied between 0.03 m and 0.06 m.

114 The lower part of the vertical profile of the mean horizontal velocity that develops above the transversal  
 115 bars can be modelled by the classic logarithmic profile:  $U(z) = (u_*/\kappa)\ln[(z-d)/z_0]$ , where  $z_0$  is the roughness  
 116 length,  $u_*$  is the friction velocity,  $d$  is the displacement height and  $\kappa$  is the Von Kármán constant. The  
 117 incoming wind profile was kept constant in this study. The free stream velocity at the top of the boundary  
 118 layer ( $U_\infty$ ) was kept fixed and equal to 4.5 m/s. The friction velocity  $u_* = 0.22$  m/s was determined from the  
 119 Reynolds stress profile, while  $z_0 = 0.1$  mm and  $d = 57$  mm were evaluated by fitting the logarithmic profile to  
 120 the experimental data in the lower part of the boundary layer flow. Note that the incoming flow corresponds  
 121 to that of Configuration 1 in [64], to which the reader is addressed for further details on the statistics of the  
 122 velocity field.

123 A pollutant release was simulated by the injection of ethane from a linear ground level source placed at  
 124 the centre of the canyon. The linear source was a porous polymeric tube with diameter  $\Phi = 4$  mm, located in  
 125 a slot cut in the tunnel floor so as not to alter the velocity field (see Figure 1.b). The tracer gas supply was  
 126 monitored continuously using a Brooks flow meter, and the experiments were performed with a mass flux of  
 127 2.8 mg/s, giving a mass flow rate per unit of length  $\dot{M}_q = 4$  mg/s·m. The fluctuations in the mass flow rate  
 128 were less than 1%.

129 To investigate buoyancy effects inside the canyon, each lateral wall of the street canyon was heated at a  
 130 time. A heating mat was attached at the back of the heated wall, inside the lateral aluminium bar (as shown  
 131 in Figure 1.c). Constant and controlled heat fluxes from the thermal resistance were produced exploiting Joule  
 132 heating.

133 Experiments with roughness elements to the side walls were performed to analyse the effect of small scale

134 geometry on the cavity flow. In these experiments, a corrugated cardboard sheet was fixed to one or the other  
 135 lateral wall of the canyon.

## 136 2.2 | Measurement techniques

137 The velocity field within the cavity and in the lowest part of the boundary layer was measured using a Particle  
 138 Image Velocimetry (PIV) system. Two coupled YAG laser sources provided pairs of laser pulses at a frequency  
 139 of 4 Hz. The visualization light sheet was perpendicular to the canyon axis and measured 1 mm in width. The  
 140 flow was seeded with micron-sized droplets produced by a smog generator. The observation field measured  
 141 approximately 0.12 m x 0.12 m (2H x 2H), and was filmed at a resolution of 1280 x 1024 pixels. Due to  
 142 the reflection of the laser light on the cavity surfaces, velocity measurements very close to the walls had  
 143 to be discarded. However, the disturbed area consisted of a thin layer of one to two millimetres near the  
 144 walls, thus not compromising the analysis of the velocity field as a whole. The images were processed using  
 145 cross-correlation. The interrogation window was fixed at 16 x 16 pixels, corresponding to an averaging area of  
 146 0.9 mm x 0.9 mm. The interrogation areas overlapped by 50% so that in total, each velocity field computation  
 147 yielded a set of 240 x 240 vectors. The velocity field was recorded with 1000 double frame images at a frequency  
 148 of 4 Hz, i.e. two images were captured each 0.25 seconds, with a time interval of 30  $\mu$ s between the two shots.  
 149 From these 1000 instantaneous velocity fields, we computed for each (x, z) point reliable flow statistics up to  
 150 the third order moment of the velocity field, as shown in Figure S1 in the Supporting Information (SI). In  
 151 this way, we obtained the horizontal (U) and vertical components (V) of the mean velocity, their variances  
 152  $\sigma_u^2$  and  $\sigma_v^2$ , and the mean vorticity field  $\bar{\omega} = (\partial V/\partial x - \partial U/\partial z)\mathbf{k}$ . The turbulent kinetic energy field (TKE)  
 153 was computed as  $\text{TKE} = 0.5(\sigma_u^2 + \sigma_v^2)$ . In this expression, the velocity variance in the third direction ( $\sigma_w^2$ ) is  
 154 missing as the velocity field is measured only in the plane perpendicular to the canyon axis. While providing  
 155 information on the spatial structure of the flow (e.g., the vorticity field), PIV system suffers some limitations  
 156 when used to elaborate the turbulence statistics, since a lower number of samples per location is available  
 157 compared to other measurement systems, as Hot Wire Anemometry (HWA) or Laser Doppler Anemometry  
 158 (LDA) [28]. Best practices were adopted to minimize the errors in the measurements [1, 60]. Moreover, we  
 159 tested the performances of the PIV system by comparing the vertical profile of TKE with measurements from  
 160 an Hot Wire Anemometer system [53]. Starting from these measurements, we estimated a percentage error  
 161 almost everywhere below 5% (with peaks of 10%) for the TKE.

162 Concentration within the cavity was measured using a Flame Ionisation Detector (FID) system [17]. FID  
 163 is commonly used for concentration measurements in urban-like geometries [e.g., 59, 12]. A FID system with a  
 164 sampling frequency of about 800 Hz [54] was used in this study, thus allowing the reconstruction of a 400 Hz  
 165 concentration signal ( $\approx 1$  ms time response of the instrument). Ethane was chosen as a passive tracer, since its  
 166 molecular weight is nearly the same of air. To avoid the disruption of the local flow, a straight 30 cm long  
 167 sampling capillary tube was mounted on the FID head, which was positioned above the test section so as not  
 168 to affect the flow field. Steady and unsteady experiments were carried out. In steady conditions, the injection  
 169 of ethane from the ground level source was kept constant and the mean concentration within the cavity was  
 170 measured on a regularly spaced grid (1 cm x 1 cm). In each sampling point, a FID acquisition time of 60  
 171 seconds was sufficient to provide averaged statistics. The mean concentration field was then obtained by spatial  
 172 interpolation between the sampling points. The experiments in unsteady conditions were performed to estimate  
 173 the typical wash-out velocity of the cavity. As in [61] and [63], we measured the temporal evolution of ethane  
 174 concentration at different positions within the cavity as it emptied. In Figure 1.d, the position of the sampling

175 points is reported. The experiment was performed as follows: (i) ethane was first injected into the canyon until  
 176 the concentration field reached a stationary state; (ii) the injection of ethane was then interrupted by means of  
 177 a valve; (iii) the temporal evolution of the concentration was recorded by the FID probe for a time interval of  
 178 15 seconds, in a single sampling point. For each sampling point, passages (i) to (iii) were repeated between 30  
 179 and 50 times to allow an ensemble average for the signal. By the subtraction of the background concentration  
 180 ( $C_b$ ) and the normalization to the initial value, i.e. the initial concentration in stationary conditions ( $C_{ss}$ ) in  
 181 the sampling point, the dimensionless (ensemble-averaged) wash-out curve was finally obtained.

182 For the experiments with heating of the side walls, two heat flux sensors of size of 3 cm x 3 cm, thickness 0.3  
 183 mm, and sensitivity  $5 \times 10^{-3} \text{ V}/(\text{W}/\text{m}^2)$  were placed on the heated wall, on the side facing the canyon (as shown  
 184 Figure 1.c). These sensors monitored the constant thermal flux at the heated wall. More details about the  
 185 heat fluxes measured during the experiments are reported in the SI. For temperature measurements, 5 T-type  
 186 thermocouples were placed on the heated wall (the position of the sensors is shown in Figure 1.c) and a single  
 187 thermocouple on the non-heated wall. Moreover, each heat flow sensor was also equipped with a thermocouple.  
 188 Temperature was measured for the entire duration of the experiment and remained on average constant over  
 189 time ( $\approx \pm 1 \text{ K}$ ). A maximum spatial difference of temperature of around  $\pm 2 \text{ K}$  degrees was observed along the  
 190 longitudinal coordinate of the wall. Negligible effects in the immediate vicinity of the walls were observed in  
 191 the flow field due to the installation of the thermocouples and the heat flux sensors.

### 192 2.3 | Experimental conditions

193 Street canyon ventilation is expected to depend on the variables that characterize the turbulent flow within  
 194 the street canyon. These are: the height ( $H$ ) and the width ( $W$ ) of the canyon cross-section, the kinematic  
 195 viscosity ( $\nu$ ) and the thermal ( $\alpha$ ) and mass ( $D$ ) diffusivity of the fluid, a characteristic velocity scale ( $\mathcal{U}$ ), the  
 196 roughness height ( $h_r$ ) of the canyon walls, the gravitational acceleration ( $g$ ), the reference air temperature  
 197 ( $T_0$ ), and the surface temperature of the possible heated wall ( $T_W$ ). Introducing the velocity  $u_d$  as the rate of  
 198 vertical bulk exchange of pollutants between the street canyon and the overlying atmosphere, we can therefore  
 199 seek to define the following dependence:

$$u_d = f(H, W, \nu, \alpha, D, \mathcal{U}, h_r, g, T_0, T_W), \quad (1)$$

200 which, according to the Buckingham  $\Pi$  theorem, can be expressed in the following non-dimensional form:

$$\frac{u_d}{\mathcal{U}} = f\left(\frac{H}{W}, \frac{h_r}{H}, Pr = \frac{\nu}{\alpha}, Sc = \frac{\nu}{D}, Re = \frac{\mathcal{U}H}{\nu}, Fr_f = \frac{\mathcal{U}}{\sqrt{gH\frac{\Delta T}{T_0}}}\right), \quad (2)$$

201 with  $\Delta T = T_W - T_0$ . The physics of the phenomenon depends on two geometrical parameters, and four  
 202 dynamical parameters. The geometrical parameters are the aspect ratio ( $H/W$ ) of the canyon cross-section  
 203 and a characteristic roughness ( $h_r/H$ ) of the canyon walls. These parameters account for the effect of large  
 204 and small geometrical scales, respectively. The three dynamical parameters are the Prandtl ( $Pr$ ), Schmidt  
 205 ( $Sc$ ), Reynolds ( $Re$ ) and internal Froude ( $Fr_f$ ) numbers. The definition of the velocity scale  $\mathcal{U}$  in the Reynolds  
 206 and Froude numbers is not trivial for a flow within a cavity. Kovar-Panskus et al. [33] and Allegrini et al. [3]  
 207 assumed  $\mathcal{U}$  as the velocity at the top of the external boundary layer flow ( $U_\infty$ ). However, this is not necessarily  
 208 a characteristic scale for the flow in the canyon since the same  $U_\infty$  could produce different boundary layer flows,

209 and therefore different canyon flows, depending on the roughness of the obstacles upwind the canyon. Other  
 210 authors [13, 68] considered as velocity scale the wind speed at the building height ( $U_H$ ). Salizzoni et al. [62]  
 211 observed that there is not a unique velocity scale that correctly characterizes the turbulent flow within the  
 212 canyon. They also found that the turbulent kinetic energy (TKE) within the cavity scales well on the friction  
 213 velocity  $u_*$ . Since the wash-out process is expected to depend on the TKE [63], we take, in this study, the  
 214 friction velocity  $u_*$  as velocity scale.

215 The Prandtl and Schmidt numbers (see Equation 2) are almost constant within the range of temperature  
 216 we consider in our experiments ( $Pr \simeq 0.7$  and  $Sc \simeq 0.9$ ). The Reynolds number undergoes slight variations due  
 217 to small differences in the velocity profile realized in the wind-tunnel and to the increase of  $\nu$  with temperature.  
 218 In wall-heated configurations, sharp temperature gradients are measured in close proximity to the heated wall  
 219 (within 0.5 cm from the wall), while the average temperature in the cavity increases by a maximum of 50 K with  
 220 respect to the temperature outside the canyon. Taking into account the increase in  $\nu$  with this temperature  
 221 variation, we obtain Reynolds numbers based on the wind speed at the building height ( $Re_H = U_H H / \nu$ ) in  
 222 the range 5700-7200. Castro and Robins [13] and Marucci and Carpentieri [44] showed that, for  $Re_H$  larger  
 223 than 4000, no Reynolds number effects were discernible for the flow field within a cavity of unit aspect ratio.  
 224 Considering a Reynolds number based on the free stream velocity ( $Re_\infty = U_\infty H / \nu$ ), Allegrini et al. [3] obtained  
 225 a Reynolds independent flow, in a square cavity, for  $Re_\infty$  above 13000. In our setup,  $Re_\infty$  is in the range  
 226 14200-18000. The narrow street canyon is expected to be more vulnerable to the  $Re$  independency. However,  
 227 Barlow and Belcher [7] found a  $Re$  independent transfer velocity in a canyon with  $H/W = 2$  for  $Re_H$  lower  
 228 than those of this experiment. After these considerations, we can therefore assume that the flow is Reynolds  
 229 independent in our experiment.

230 The experiments were performed for aspect ratios varying between 1 and 2. These are the typical geometries  
 231 in European urban environments [73]. The effect of roughness on the canyon walls was tested by adding small  
 232 scale roughness elements on one or the other sidewall. Experiments with two different roughness scales ( $h_r$ ) were  
 233 performed: corrugated cardboard sheets with flute thickness of 2 mm ( $h_r/H = 1/30$ ) and 5 mm ( $h_r/H = 1/12$ )  
 234 were used to simulate an idealised façade roughness. Notice that a roughness scale of 5 mm on the 60 mm  
 235 high canyon wall is representative of a characteristic balcony depth of 1.5 m in a street canyon with 20 m  
 236 high side buildings [e.g. 49]. Three heating configurations were investigated: (i) the isothermal case, (ii) the  
 237 heating of the upwind (UW) wall, and (iii) the heating of the downwind (DW) wall. In the last two cases,  
 238 different thermal fluxes were imposed at the heated wall. The resulting temperature differences ( $\Delta T = T - T_0$ )  
 239 are reported in Table 1, with the corresponding  $Fr_f$ . The reference temperature  $T_0$  ( $T_0 \simeq 300$  K) varied from  
 240 day to day, and was measured away from the street canyon.

241 It is worth noting that, since the velocity scale is different, the values of  $Fr_f$  considered here cannot be  
 242 directly compared to those of Kovar-Pankus et al. [33], Allegrini et al. [3], and Marucci and Carpentieri [44].  
 243 However, taking  $U_\infty$  as velocity scale in order to compare the conditions of the different experiments, we obtain  
 244  $Fr_f$  values of an order of magnitude higher than those obtained in the above mentioned works, since the size of  
 245 the canyon in our experiments is considerably smaller. Taking the Froude number as similarity criterion, our  
 246 experimental conditions correspond to temperature differences from 4 to 15 Kelvin degrees in realistic street  
 247 canyons flanked by 20-meter high buildings, and subject to a wind profile characterized by  $u_* = 1$  m/s. These  
 248 temperature differences are typically reached near sun-heated walls in Mediterranean cities [43, 55].

$\frac{H}{W}$	No Roughness						Roughness		
	No Heating	DW Heating ( $\Delta T$ ) [K]				UW Heating ( $\Delta T$ ) [K]		UW	DW
		70	140	170	240	140	240		
1	✓	$Fr_i = 0.62$	X	$Fr_i = 0.40$	$Fr_i = 0.34$	$Fr_i = 0.44$	$Fr_i = 0.34$	✓	✓
1.5	✓	$Fr_i = 0.57$	$Fr_i = 0.40$	$Fr_i = 0.37$	$Fr_i = 0.31$	$Fr_i = 0.45$	$Fr_i = 0.34$	✓	✓
1.3, 1.4, 1.6, 1.7, 1.8, 2	✓			X			X	✓	✓

TABLE 1 Experimental configurations. The check mark indicates the investigated experiments, while the X marks those not considered. The internal Froude number is specified for the configurations with differential heating of the walls. UW and DW stand for Upwind and Downwind wall, respectively.

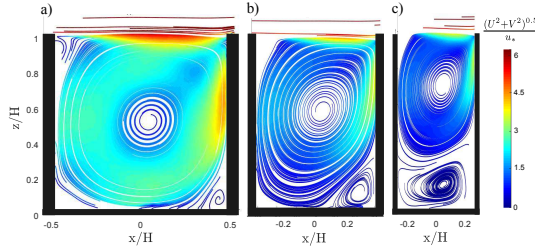


FIGURE 2 Streamlines of the mean velocity field for the aspect ratios (a)  $H/W=1$ , (b)  $H/W=1.5$  and (c)  $H/W=2$ .

### 249 3 | EFFECT OF LARGE AND SMALL GEOMETRICAL SCALE

#### 250 3.1 | Effect of the large geometrical scale

251 As well documented by previous experimental and numerical studies [45, 27, 56, 67], the topology of the mean  
 252 velocity streamlines within the cavity varies with the canyon geometry. In our experiments, the mean flow  
 253 shows that, for an aspect ratio  $H/W$  equal to 1, most of the cavity is filled by a large rotating cell, with its  
 254 centre close to the cavity centre (Figure 2.a). As the street aspect ratio increases, a second counter-rotating  
 255 cell appears at the bottom of the cavity (Figure 2.b-c). The velocities in this second vortex are much lower  
 256 than those in the upper vortex. In our experiments, the transition from one main circulating cell to two  
 257 counter-rotating cells emerges for an aspect ratio  $H/W$  greater than 1.8. For this aspect ratio, the sign of the  
 258 vertical velocity profile in  $x = 0$  (Figure 3) changes three times, revealing that the second cell is fully established  
 259 in the centre of the lower part of the canyon. A similar value (i.e.  $H/W = 1.7$ ) was found numerically by Sini  
 260 et al. [67], while Lee and Park [35] found that this transition takes place for  $H/W \approx 2.1$ . As will be discussed  
 261 below, this transition depends on the amount of clockwise vorticity entering the canyon, i.e. on the approaching  
 262 flow as well as on the cavity aspect ratio. This explains why discrepancies on the  $H/W$  value for transition  
 263 occur in the different studies.

264 In all the considered geometries, the turbulent kinetic energy within the cavity (Figure 4) is up to an  
 265 order of magnitude lower than in the external flow (i.e. for  $z/H > 1$ ). This finding is in accordance with the  
 266 experimental results obtained by Salizzoni et al. [62], Allegrini et al. [3] and Marucci and Carpentieri [44].  
 267 In the here analysed configurations, the transversal bars are very close, so that the flow regime in the street  
 268 canyon is a skimming flow [56]. In skimming flow, the size of the turbulent eddies that develop in the shear  
 269 layer at the top of the cavity is limited to the horizontal spacing between the obstacles. Therefore, the eddies

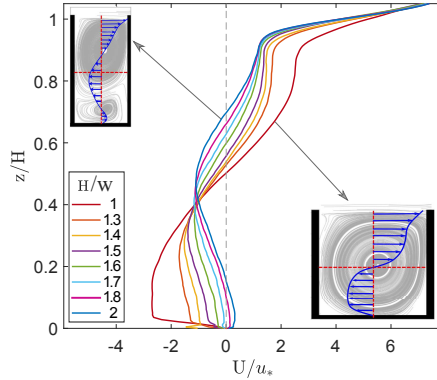


FIGURE 3 Vertical profile of the mean horizontal velocity at  $x = 0$  for different aspect ratios.

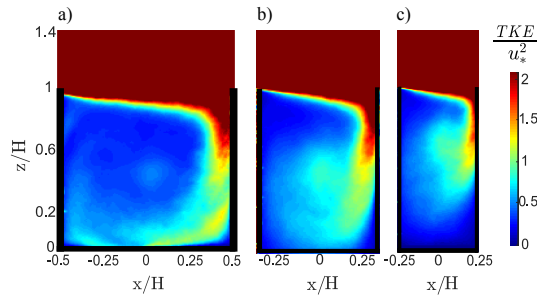


FIGURE 4 Turbulent kinetic energy for the aspect ratios (a)  $H/W=1$ , (b)  $H/W=1.5$  and (c)  $H/W=2$ .

270 in the shear layer are not sufficiently developed to couple with the turbulent eddies in the external flow [e.g.,  
 271 37, 62]. As a consequence, the shear layer shelter the flow within the cavity and the fluctuating flow within  
 272 the canyon is isolated from the external flow. The main interaction between the cavity flow and the external  
 273 flow is confined to the upper edge of the downwind wall. Here, a TKE plume spreads down into the cavity  
 274 all along the canyon wall. For a square cavity, the plume reaches the downwind lower corner and it affects  
 275 the entire cavity at the street level (panel a in Figure 4). With increasing aspect ratios, the formation of the  
 276 second counter-rotating cell inhibits the turbulence transfer in the lower part of the canyon (panel c).

277

278 The formation of the second cell can be conveniently described in terms of vorticity more readily than in  
 279 terms of velocity. The vorticity transport equation for a zero-divergence flow is

$$\frac{D\boldsymbol{\omega}}{Dt} = \boldsymbol{\omega} \cdot \nabla \mathbf{u} + \nu \nabla^2 \boldsymbol{\omega} - S_T \times \mathbf{g}, \quad (3)$$

280 where  $\boldsymbol{\omega}$  is the vorticity,  $\mathbf{g}$  is the gravity vector, and  $S_T$  is a function of the temperature gradient:  $S_T = \nabla T/T$ .  
 281 The rate of change of vorticity (on the left-hand side of Equation 3) is therefore given by the stretching of

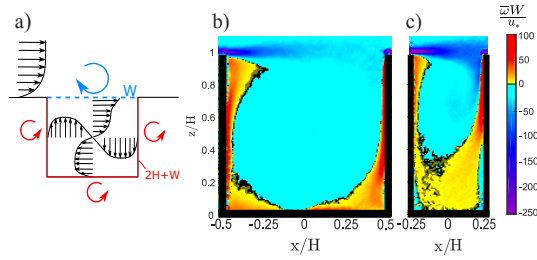


FIGURE 5 a) Qualitative representation of the mean velocity profile inside the cavity and of the vorticity boundary conditions. b-c) Vorticity field inside the cavity for aspect ratios  $H/W = 1$  and  $H/W = 2$ .

282 vorticity due to flow velocity gradients (first term on the right-hand side), the diffusion of vorticity due to the  
 283 viscous effects (second term on the right-hand side), and vorticity changes due to thermal gradients (last term  
 284 of Equation 3). This latter is a source term given by the vector product between the thermal gradient and the  
 285 gravity vector. Equation 3 is completed by appropriate vorticity conditions at boundaries [e.g., 6, 58]. The  
 286 main features of these boundary conditions can be grasped by observing the qualitative profile of the mean  
 287 velocity at the four boundaries of the domain (Figure 5.a). The boundary layer that occurs along the walls of  
 288 the cavity generates anticlockwise vorticity. Conversely, the shear layer at the top of the cavity generates a  
 289 Kelvin-Helmholtz type instability leading to the formation of large-scale clockwise vortices that are entrained  
 290 into the cavity. The same vorticity dynamics in a square cavity-driven flow were observed numerically [15, 66]  
 291 and experimentally [40, 47] in previous works. To readily understand how the vorticity balance changes in a  
 292 narrow cavity compared to a square one, a geometry-based interpretation is suggested. Given a constant height  
 293  $H$  of the canyon, the exchange surface ( $W$ ) between the external flow and the canyon decreases when the aspect  
 294 ratio  $H/W$  increases. As a consequence, the clockwise vorticity advected inside the cavity decreases as the  
 295 cavity narrows. The anticlockwise vorticity at walls can be assumed proportional to the solid perimeter of the  
 296 cavity ( $2H + W$ ). This perimeter also decreases as  $H/W$  increases, but less rapidly than  $W$ . Consequently, as  
 297 the aspect ratio increases, a surplus of anticlockwise vorticity accumulates at the bottom of the cavity (Figure  
 298 5.c) and a second counter-rotating cell generates.

299 Note that assuming a change in the aspect ratio from 1 to 2 due to a doubling of  $H$  instead of a halving of  $W$ ,  
 300 the Reynolds number would double for the narrow cavity. In this case, changes in the vorticity balance due to  
 301 different flow conditions are expected. Thus, the above presented geometry-based interpretation is valid under  
 302 the hypothesis of a constant Reynolds number for the two geometries.

303 After the analysis of the flow field within the cavity, we present below the results about the effect of the  
 304 canyon geometry on pollutant dispersion. Figure 6 shows the concentration field of the passive scalar released by  
 305 the ground level source in stationary conditions. The non-dimensional concentration is expressed as  $Cu_*H/M_q$ ,  
 306 where  $C$  is the time averaged concentration of ethane, and  $M_q$  is the mass flow injected at the linear source per  
 307 unit of length (see Section 2.2). Figure 6.a evidences the presence of a fresh air plume entering the square cavity  
 308 at the upper corner of the downwind wall. As the aspect ratio of the cavity increases, higher concentrations of  
 309 pollutants are measured at the pedestrian level compared to the mean concentration in the square cavity. For  
 310 a cavity with  $H/W = 2$  (Figure 6.c), the concentration at street level is up to three times the concentration in  
 311 the centre of the cavity. Thus, the formation of the second cell inhibits the transfer of pollutants from street  
 312 level to the external flow, as already found by Hussain and Lee [27], Oke [56], and Jeong and Andrews [30].  
 313 Moreover, we observe a different horizontal distribution of the mean concentration at street level in the two

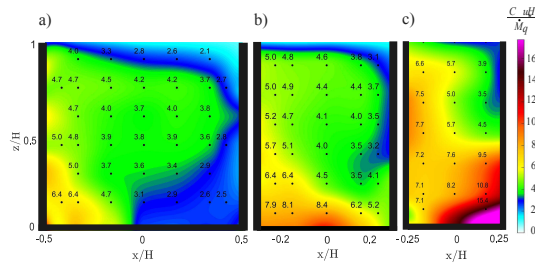


FIGURE 6 Mean concentration of the passive scalar inside the cavity for the aspect ratio (a)  $H/W = 1$ , (b)  $H/W = 1.5$  and (c)  $H/W = 2$ .

314 geometries. When the fresh air plume reaches the street level (for  $H/W=1$ ), pollutant concentration at the  
 315 lower left corner is double compared to the right corner. Conversely, for  $H/W=2$ , ‘air quality’ is worse at the  
 316 lower right corner with concentrations that are, also in this case, two times the concentrations measured at the  
 317 other corner. This spatial distribution of the mean concentration for square and narrow cavities is in accordance  
 318 with previous studies [5, 4, 41]. In particular, the numerical simulations of Assimakopoulos et al. [4] and Liu  
 319 et al. [41] showed similar values for the ratio of the concentrations measured in the two lower corners of the cavity.  
 320

321 The above presented results are confirmed by the analysis of the exchange processes inside the canyon for  
 322 the different geometrical configurations. To this aim, the wash-out curves from the unsteady experiments (see  
 323 Section 2.2) are considered.

324 In Figure 7, the wash-out curves measured at different positions for both a square (panel a) and a narrow  
 325 (panel b) cavity are reported. For each sampling point (points *a* to *e* in the insets in Figure 7), the wash-out  
 326 curve is normalized by the mean concentration measured at that position in stationary conditions ( $C_{ss}$ ). We  
 327 observe that for both geometries all curves have an horizontal tangent for  $t \rightarrow 0$ . As discussed by [63], this  
 328 feature is not consistent with a one-degree of freedom model, based on the assumption of a perfect mixing  
 329 within the canyon. In this sense the horizontal tangent indicates an initial mixing process acting on the  
 330 non-uniform concentrations within the canyon. Moreover, the curves follow two characteristic trends depending  
 331 on the position of the sampling point. In the square cavity (panel a), the time delay before the concentration  
 332 decay is longer for the curve registered at the centre of the cavity (point *a*) with respect to those measured in  
 333 the recirculating part of the flow (points *b-e*). The trend of these latter curves is very similar, instead. In the  
 334 narrow cavity (panel b), the concentration in the upper part of the cavity (points c-e) decays later than in the  
 335 bottom part of the cavity (points *a-b*). The exchange between a street canyon and the atmosphere aloft is  
 336 traditionally described with box models with one degree of freedom [e.g., 25, 31, 8, 71, 34, 14]. In these simple  
 337 models, the canyon is described as a box with uniform pollutant concentration and a discontinuity surface at  
 338 the top, where the exchange takes place. However, the mean concentration field in Figure 6 and the wash-out  
 339 curves shown in Figure 7 depict a different picture. The mean concentration is far from being uniform within  
 340 the canyon and the wash-out curves are not identical in all the regions of the flow. These two features evidence  
 341 how the rate of pollutant transfer is not uniform inside the cavity and that more than one time scale is involved  
 342 in the wash-out process. Since these experimental data cannot be interpreted with a box model with a single  
 343 degree of freedom, we apply the analytical model with two degrees of freedom proposed by [61], [63], and [48].  
 344 According to this model, the wash-out mechanism is described as a sequence of transfers between three regions,

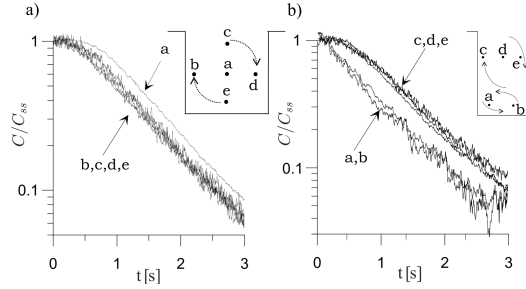


FIGURE 7 Dimensionless wash-out curves measured at different positions within a (a) square cavity with aspect ratio  $H/W = 1$  and (b) a narrow cavity with aspect ratio  $H/W = 2$ .

345 each one with a different mean concentration (see Figure S1 in the SI). One region represents the external  
 346 flow, while the two other regions give a rough description of pollutant distribution inside the canyon. In a  
 347 cavity with a single main recirculating cell (as the square cavity in Figure 7.a), the first region (box<sub>1</sub>) is the  
 348 recirculating part of the flow, while the second region (box<sub>2</sub>) is the core of the flow within the main vortex.  
 349 The distinction between these regions is consistent with the different behaviour observed in Figure 7.a for the  
 350 wash-out curve in point *a* with respect to the trend in points *b-e*. In a cavity with two recirculating cells  
 351 (as the narrow cavity in Figure 7.b), the two regions are the cells at the top (box<sub>1</sub>) and at the bottom (box<sub>2</sub>) of  
 352 the cavity, in accordance with the two trends observed in Figure 7.b for the concentration measured in points  
 353 *c-e* and *a-b*, respectively.

354 For both a square and a narrow cavity, the model with two degrees of freedom is given by a system of  
 355 two differential equations (Equation S2 in the SI). This system admits as solution the analytical wash-out  
 356 curves  $C_1(t, u_d, \tilde{u}_d)$  and  $C_2(t, u_d, \tilde{u}_d)$  (Equation S9 in the SI) that describe the temporal evolution of the mean  
 357 concentration in box<sub>1</sub> and box<sub>2</sub> as a function of two free parameters,  $u_d$  and  $\tilde{u}_d$ . The velocity  $u_d$  is the bulk  
 358 exchange velocity between box<sub>1</sub> and the external flow, while  $\tilde{u}_d$  is the bulk exchange velocity between box<sub>1</sub>  
 359 and box<sub>2</sub>. The least squared method is applied to find the values of  $u_d$  and  $\tilde{u}_d$  that minimize the difference  
 360 between the experimental data and the analytical curves.

361 In Figure 8, the analytical wash-out curves are compared with the experimental data for a square (panel a)  
 362 and a narrow cavity (panel b). The good agreement between data and model demonstrates that the simplified  
 363 two-box model gives a satisfactory description of the cavity wash-out. For both geometries, the estimated  
 364 velocities  $u_d$  and  $\tilde{u}_d$  are reported. These results show that, for a narrow cavity,  $u_d$  is more than twice  $\tilde{u}_d$ . The  
 365 effective transport of pollutant particles from the bottom cell to the upper cell within the cavity is slow, while  
 366 the wash-out towards the external atmosphere is rapid. Since pollutant release takes place at the pedestrian  
 367 level, this slower transfer acts as a bottleneck for the entire ventilation process and a higher concentration  
 368 develops at street level (Figure 6.c). Conversely, in a square cavity, pollutants emitted at street level are  
 369 directly transferred outside with velocity  $u_d$ . In this case, the low  $\tilde{u}_d$  value reduces the transfer rate in the  
 370 centre of the cavity with no significant effects on the street level dynamics.

371 Since the transition from one to two recirculating cells is crucial for the spatial distribution and the  
 372 concentration of pollutants inside the cavity, in the following sections we will discuss the effect of wall roughness  
 373 and heating on this transition.

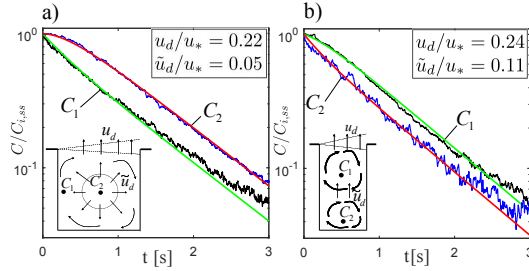


FIGURE 8 a) Experimental (black and blue lines) and analytical (green and red lines) wash-out curves in the recirculating region and in the centre of a square cavity. b) Experimental (black and blue lines) and analytical (green and red lines) wash-out curves at the top and the bottom of a narrow cavity. For both aspect ratios, the wash-out velocities ( $u_d$  and  $\bar{u}_d$ ) are reported.

### 374 3.2 | Effect of the small geometrical scale

375 Experiments with two different roughness scales ( $h_r = 2$  mm and  $h_r = 5$  mm) at the lateral walls of the canyon  
 376 were performed. Only the results obtained for roughness elements 5 mm high are shown and discussed here. A  
 377 similar, but less pronounced, behaviour was observed with small roughness elements.

378 Figures 2 and 3 evidenced that, for a cavity with smooth walls, the aspect ratio  $H/W = 3/2$  is close to the  
 379 critical ratio for transition. For this geometry, the occurrence of roughness elements (with  $h_r = 5$  mm) on the  
 380 upwind wall of the cavity has slight effects on the mean velocity field (see Figure 9.a compared to Figure 2.b).  
 381 Conversely, adding roughness to the downwind wall facilitates the formation of the second counter-rotating  
 382 cell. In fact, the streamlines in Figure 9.b reveal an incipient separation between the regimes of motion in  
 383 the upper and lower part of the cavity. This behaviour is confirmed for different aspect ratios by the analysis  
 384 of the vertical profile of the mean horizontal velocity in  $x = 0$  (Figure 9.c). With roughness elements on the  
 385 upwind wall (dashed lines), the vertical profile slightly differs from the profile that is established in the cavity  
 386 with smooth walls (dotted lines). With roughness on the downwind wall (continuous line) the vertical profile  
 387 tends to the characteristic profile of a motion with two counter-rotating cells, as those observed in Figure 3 for  
 388 aspect ratios greater than 1.8.

389 As for the large geometrical scale, the effect of wall roughness can be interpreted in terms of vorticity.  
 390 Wall roughness increases the mean velocity gradients near the walls. As a consequence, the vorticity flux  
 391 from the wall towards the cavity (Figure 5.a) is enhanced. However, for a rough upwind wall, the additional  
 392 anticlockwise vorticity is more rapidly transferred outside the cavity, so that it does not significantly modify  
 393 the vorticity balance in the domain. This is evidenced by panels d and e in Figure 9 showing the vorticity  
 394 field in a cavity with aspect ratio  $3/2$  with smooth walls and with roughness elements on the upwind wall,  
 395 respectively. On the other hand, the additional anticlockwise vorticity generated at the rough downwind wall  
 396 is advected along the streamlines of the mean velocity field in the core of the cavity, where it induces the  
 397 formation of the counter-rotating cell. The increase in anticlockwise vorticity at the bottom of the cavity can  
 398 be observed in the case of roughness elements on the downwind wall in Figure 9.f.

399 The formation of secondary vortices in the street canyon due to the presence of roughness elements on  
 400 building walls is confirmed by the numerical studies of Murena and Mele [49] and Llaguno-Munitxa et al. [42],  
 401 who observed a reduced turbulence intensity and a slower wash-out of the cavity. However, these numerical  
 402 studies did not analyse the effect of roughness on one wall at a time.

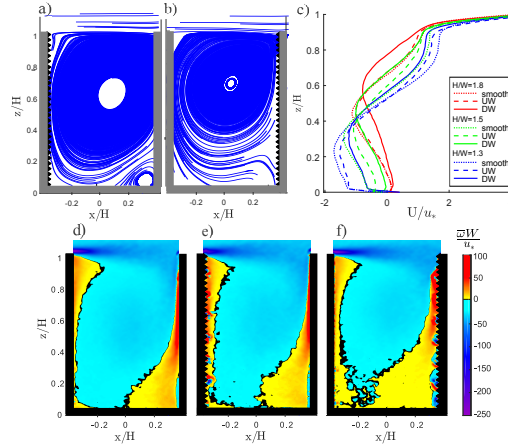


FIGURE 9 Effect on the mean velocity field of wall roughness at the (a) upwind (UW) and (b) downwind (DW) wall for a cavity with  $H/W = 3/2$ . (c) Vertical profile of the mean horizontal velocity in  $x = 0$  for different aspect ratios and for different conditions of the walls: smooth walls (dotted lines), UW roughness (dashed lines) and DW roughness (continuous lines). Normalized vorticity field within a cavity with  $H/W=3/2$  and with (a) smooth walls, (b) UW wall roughness, (c) DW wall roughness.

## 403 4 | EFFECT OF WALL HEATING

### 404 4.1 | Effect of upwind wall heating

405 The upwind wall of the cavity is heated and three temperature differences ( $\Delta T$ ) are experimented and discussed:  
 406 0 K, 140 K, and 240 K (Froude numbers are reported in Table 1). The effect of wall heating is investigated  
 407 for a square cavity ( $H/W = 1$ ) and for a narrow cavity with an aspect ratio  $H/W = 3/2$ . As observed in the  
 408 previous sections, in this latter geometrical configuration the flow field is close to the transition from one to  
 409 two recirculating cells.

410 Regardless the wall temperature, the mean velocity profiles (panels a and b in Figure 10) evidence the  
 411 presence of a shear layer at the cavity top, where the vertical profile of the horizontal component (black lines)  
 412 reaches its maximum. The level of TKE (panels c and d in Figure 10) is higher at the cavity top and along the  
 413 downwind wall, where a TKE plume spreads down in the cavity from the external flow.

414 We observe negligible variations in the mean and fluctuating velocity fields, when the upwind wall is heated.  
 415 This is found for both a square (panels a and c in Figure 10) and a narrow (panels b and d Figure 10) cavity.  
 416 Other authors [e.g., 3, 44] found a slight increase of the mean motion and of the TKE inside a square cavity  
 417 due to buoyancy effects at the upwind wall. This is likely to be due to the lower internal Froude number  
 418 considered in their experiments, that, as mentioned in Section 2.3, is one order of magnitude lower than the  
 419  $Fr_j$  values experimented here.

### 420 4.2 | Effect of downwind wall heating

421 The downwind wall of the cavity is heated and four temperature differences ( $\Delta T$ ) are considered: 0 K, 70 K,  
 422 170 K and 240 K (Froude numbers are reported in Table 1). When the downwind wall is heated, we observe

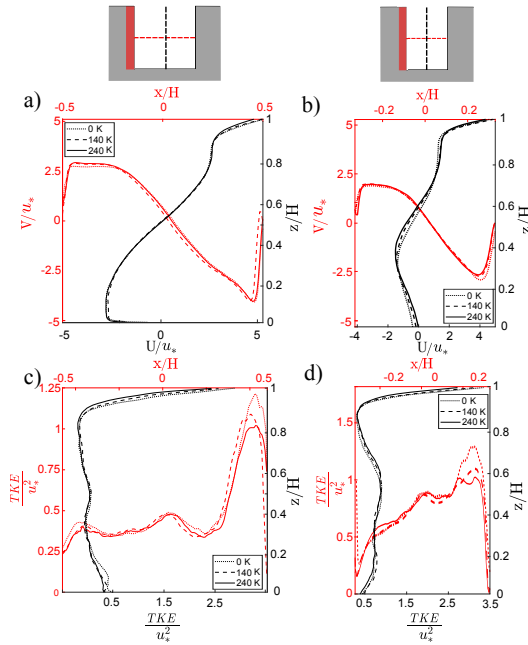


FIGURE 10 Upwind wall heating. Horizontal (red lines) and vertical (black lines) profiles of the vertical ( $V$ ) and horizontal ( $U$ ) components of the mean velocity (panels a and b) and of the TKE (panels c and d) within the cavity for the aspect ratios  $H/W = 1$  (left panels) and 1.5 (right panels).

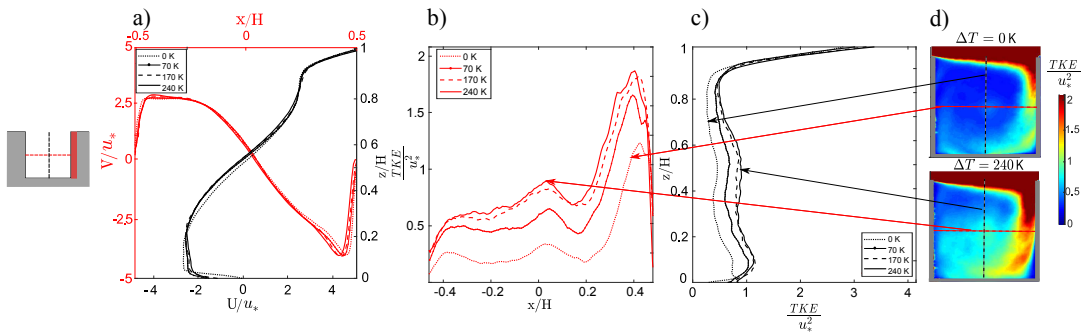


FIGURE 11 Downwind wall heating for a square cavity ( $H/W = 1$ ). Horizontal (red lines) and vertical (black lines) profiles of the vertical ( $V$ ) and horizontal ( $U$ ) components of the mean velocity (a) and of the TKE inside the cavity (b and c). In d, the TKE field for the maximum heating configuration is compared to the configuration with no heated walls.

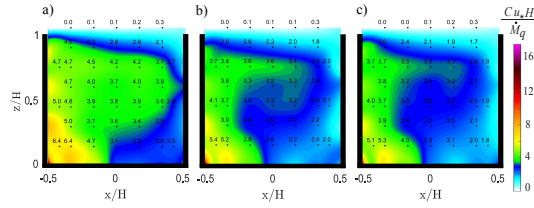


FIGURE 12 Concentration of a passive scalar released at street level in a square cavity for different heating of the downwind wall: (a)  $\Delta T = 0$  K, (b)  $\Delta T = 70$  K, and (c)  $\Delta T = 170$  K.

423 diverse effects depending on the aspect ratio of the cavity.

424

425 For square cavities ( $H/W = 1$ ), in the range of  $Fr_i$  considered in this study, the heating of the downwind  
 426 wall has negligible effects on the mean velocity field. Figure 11.a shows the vertical profile of the mean  
 427 horizontal velocity ( $U$ ) and the horizontal profile of the vertical velocity component ( $V$ ). The profiles at different  
 428 temperature configurations tend to overlap. In the SI, more results about the mean vertical velocity field for  
 429 these configurations are reported. The heating of the downwind wall has evident effects on the fluctuating  
 430 field, instead. An increment of around 400% and 200% is observed for the horizontal (Figure 11.b) and vertical  
 431 (Figure 11.c) profiles of the TKE when  $\Delta T$  increases from 0 to 240 K. These variations are significantly higher  
 432 than the error associated to the estimate of the TKE by means of PIV (see Section 2.2). Even for the TKE  
 433 variations measured for  $\Delta T = 70$  K and 170 K, the measurement error is negligible. While the variation from  
 434  $\Delta T = 170$  K to 240 K is subject to the greatest degree of uncertainty. For a square cavity, this increase in the  
 435 turbulent fluctuations near the heated downwind wall is confirmed by the studies of Allegrini et al. [3] and  
 436 Marucci and Carpentieri [44]. However, with respect to our findings, they also observed a different mean flow  
 437 structure with the formation of a secondary rotating vortex, due to the lower values of  $Fr_i$  imposed in their  
 438 experiments.

439 The mean concentration of pollutants inside the cavity decreases with increasing  $\Delta T$  when  $H/W = 1$  (Figure  
 440 12). This suggests a more efficient canyon ventilation. To further explore this behaviour, as customary, we turn  
 441 to the analysis of the wash-out curves provided by the unsteady experiments. In Figure 13, the concentration  
 442 in both the lateral (panel a) and central (panel b) part of the cavity decays more rapidly as the thermal flux at  
 443 the downwind wall is increased. The wash-out velocities (Table 2), estimated by the application of the model  
 444 with two degrees of freedom, reveal that the heating of the downwind wall enhances the wash-out velocities,  $\bar{u}_d$   
 445 and  $u_d$ . Notice that the results for  $\Delta T = 240$  K are here not reported as the experiments in unsteady conditions  
 446 for this configuration were not performed.

447 Thus, for a square cavity, the heating of the downwind wall increases the levels of TKE within the cavity  
 448 and enhances the canyon ventilation, while the mean motion is almost unaltered. Moreover, the values of the  
 449 estimated wash-out velocities ( $u_d$  and  $\bar{u}_d$ ) are very low compared to the characteristic velocity scale for the  
 450 mean advection in the cavity. These findings are in accordance with previous works [63] suggesting that the  
 451 cavity wash-out, in a perpendicular street canyon, is mainly regulated by the fluctuating component of the  
 452 velocity field. These considerations will be discussed in detail in Section 5.

453

454 In narrow cavities ( $H/W = 1.5$ ), the heating of the downwind wall has remarkable effects on both the mean  
 455 motion (panels a to c in Figure 14) and the TKE inside the cavity (panels d to g in Figure 14). The thermal

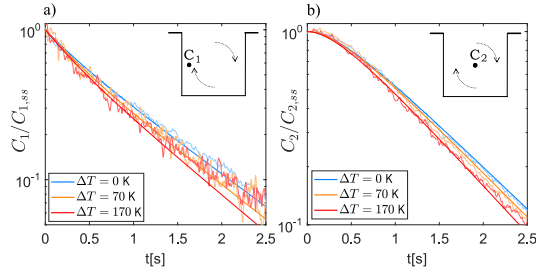


FIGURE 13 Dimensionless wash-out curves measured in the (a) lateral and (b) central part of a square cavity for different heating of the downwind wall. The analytical wash-out curves are above the experimental data (shaded lines).

TABLE 2 Variation of the wash-out velocities ( $u_d$  and  $\bar{u}_d$ ) as a function of the temperature difference  $\Delta T$  in a square cavity.

	$\Delta T = 0$ K	$\Delta T = 70$ K	$\Delta T = 170$ K
	$Fr_i = \infty$	$Fr_i = 0.62$	$Fr_i = 0.40$
$u_d/u_*$ [-]	0.22	0.33	0.35
$\bar{u}_d/u_*$ [-]	0.050	0.066	0.069

456 gradient near the downwind wall facilitates the transition from one cell to two counter-rotating cells (panel c).  
 457 This behaviour is evidenced by the vertical profile of the mean horizontal velocity in  $x = 0$  (panel b) that tends  
 458 to the characteristic profile of a motion with two counter-rotating cells as  $\Delta T$  increases and  $Fr_i$  decreases (see  
 459 the cases of  $H/W \geq 1.8$  in Figure 3). As seen in Figure 4, this transition inhibits the penetration of the TKE  
 460 plume from the external flow into the cavity. Thus, the highest values of TKE at street level are reached for  
 461 the no-heated configuration (dotted line in Figure 14.e): as the temperature of the wall increases, the level of  
 462 TKE enhances in the upper part of the canyon (panel d) while a low turbulence region develops at street level  
 463 (panel e). As pointed out for the square cavity, the uncertainty in TKE measurements by means of PIV does  
 464 not compromise the reliability of the observed trends.

465 In this configuration, the role of TKE on canyon ventilation, compared to the role of advection, can hardly  
 466 be distinguished. Here, the topology of the mean flow has an evident effect on the distribution of the TKE  
 467 and thus on canyon ventilation. However, the role of TKE in the pollutant transfer (found above for a square  
 468 cavity) is in accordance with the results obtained here for a narrow cavity. The enhancement of the turbulent  
 469 fluctuations in the upper part of the cavity (Figure 14.d) accelerates wash-out of pollutants at roof level,  
 470 while the decreasing TKE levels in the bottom part of the cavity (Figure 14.e) inhibits the vertical transfer  
 471 of pollutants from street level. Since the pollutant source is placed at street level, the slowing down of the  
 472 transfer in the lower part of the cavity acts as a bottleneck for the entire ventilation process and thus, in steady  
 473 conditions, the concentration of pollutants at street level increases with the temperature of the downwind wall  
 474 (Figure 15.c). In the SI, we further discuss the possible role of the mean motion (compared to the TKE) in  
 475 canyon ventilation.

476 As shown for the square cavity (see Figure 13 and Table 2), the analysis of the wash-out process would

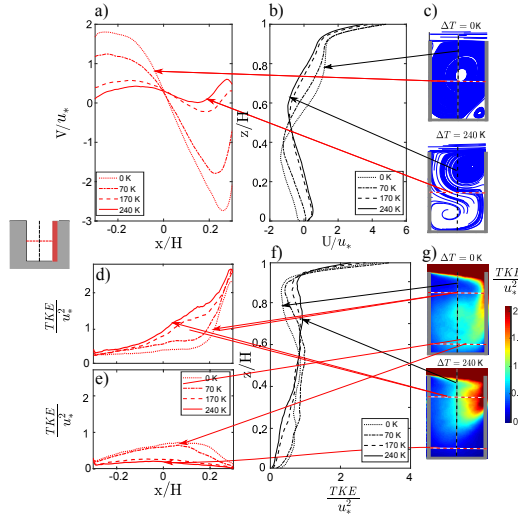


FIGURE 14 Downwind wall heating for a narrow cavity ( $H/W = 1.5$ ). Horizontal (red lines) and vertical (black lines) profiles of the vertical ( $V$ ) and horizontal ( $U$ ) components of the mean velocity (a and b) and of the TKE (d to e) inside the cavity. In panels c and g, the mean velocity field and the TKE field for the configuration with  $\Delta T = 240$  K is compared to the configuration with  $\Delta T = 0$  K.

477 provide further insights into the transport mechanisms. However, for the cavity with  $H/W = 1.5$  the analytical  
 478 model for the wash-out process is not useful for comparing the different configurations. In fact, for  $\Delta T = 0$   
 479 K, the model for a square cavity should be applied since a single vortex establishes in the cavity (see panel  
 480 c in Figure 14). For  $\Delta T = 170$  K, two distinct vortices can be identified and thus the model with two boxes  
 481 connected in series has to be used. In the transition ( $\Delta T = 70$  K) neither of the two models is applicable since  
 482 we cannot clearly identify the spatial extent of the two cells.

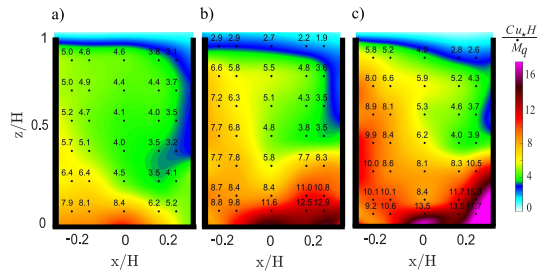


FIGURE 15 Concentration of a passive scalar released at street level in a narrow cavity for different heating of the downwind wall: a)  $\Delta T = 0$  K, b)  $\Delta T = 70$  K, and c)  $\Delta T = 170$  K

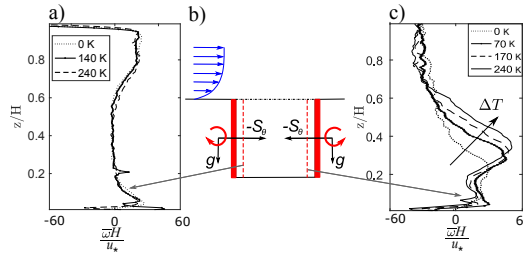


FIGURE 16 Schematic representation of the vorticity generation near the heated walls (b). Vertical profile of the vorticity near the upwind (a) and downwind (b) walls for a square cavity in the case of upwind wall heating and downwind wall heating, respectively.

### 483 4.3 | Vorticity dynamics in a heated cavity

484 As for the role of aspect ratio and wall roughness (Section 3), the analysis of the vorticity dynamics within the  
 485 cavity helps in clarifying the different flow behaviours observed for the heating of the upwind and  
 486 downwind wall (Sections 4.1-4.2).

487 In the vorticity transport equation (Equation 3), the last term accounts for vorticity production due to  
 488 thermal gradients. When the upwind wall is heated, the vector product between the opposite of the thermal  
 489 gradient  $S_T$  and the gravity vector generates clockwise vorticity near the wall (Figure 16.b). This additional  
 490 vorticity is in accordance with the main vorticity field inside the cavity and, due to geometrical reasons, it is  
 491 rapidly transferred outside the cavity with negligible effects on the mean and fluctuating velocity components.  
 492 Indeed, the vorticity near the upwind heated wall in a square cavity (Figure 16.a) exhibits a vertical profile  
 493 with negligible variations for different buoyancy conditions.

494 Conversely, when the downwind wall is heated, the thermal gradient generates anticlockwise vorticity near  
 495 the wall (Figure 16.b). Figure 16.c evidences a trend toward positive and thus anticlockwise vorticity near the  
 496 downwind heated wall of a square cavity. Similarly to the case of a rough downwind wall (section 3.2), the  
 497 additional anticlockwise vorticity generated at the wall is advected in the core of the flow field. For a square  
 498 cavity, this additional anticlockwise vorticity seems to only affect the fluctuating velocity field (Figure 11b-d),  
 499 while, in a narrow cavity, it triggers the formation of the second cell (Figure 14a-c).

## 500 5 | TURBULENT KINETIC ENERGY AND CANYON VENTILATION

501 The experimental results reported in Section 4.2 suggest a correlation between the increase in turbulent  
 502 kinetic energy and the velocity of the wash-out process in an idealised 2D street canyon perpendicular to the  
 503 wind direction. In the square cavity, TKE levels enhance within the entire cavity due to the heating of the  
 504 downwind wall. At the same time, an acceleration is observed in the pollutant exchange between the cavity  
 505 and the external atmosphere ( $u_d$ ), and between the core and the outer part of the recirculating cell within the  
 506 cavity ( $\tilde{u}_d$ ). In the narrow cavity instead, thermal fluxes at the downwind wall induce the formation of two  
 507 counter-rotating cells, and thus the TKE increases at the top of the cavity but decreases at street level. The  
 508 results for the concentration field suggest that the vertical exchange at roof level ( $u_d$ ) is accelerated, while the  
 509 exchange between the two internal cells ( $\tilde{u}_d$ ) is inhibited.

510 Our interpretation for this higher efficiency of the turbulent transport in the ventilation of the perpendicular

511 canyon is that this mechanism is responsible for the transfer of pollutant particles across the streamlines of  
512 the flow, in a dispersive motion that actually allows the particles to be intercepted by the shear layer at the  
513 roof top and brought outside the cavity. This interpretation is in line with the analysis of Salizzoni et al. [63].  
514 In this previous work, the wash-out time varied with the intensity of the turbulent fluctuations within the  
515 cavity, induced in turn by a variation of the flow statistics of the external flow. Here, we are instead keeping  
516 the external flow unaltered but we are modifying the conditions within the cavity.

517 In lights of the present experimental results and of the analysis proposed in [63], we further investigate in  
518 this Section the dependency of the wash-out velocity on the fluctuating component of the turbulent flow. To  
519 this aim, we first estimate the velocities  $u_d$  and  $\bar{u}_d$  for all the experimental configurations in which the model  
520 with two degrees of freedom can be applied, i.e. the configurations in which only one or two vortices are clearly  
521 established in the cavity. These include the experiments in a square cavity with different heat fluxes at the  
522 downwind wall (cases 1 to 3 in Figure 17), and the case of an isothermal cavity with aspect ratio  $H/W = 2$  (case  
523 7). For  $H/W = 3/2$ , we consider the configurations with  $\Delta T = 0$  K (the flow field has a single-vortex structure),  
524  $\Delta T = 140$  K and  $\Delta T = 170$  K (the flow field has a two-vortex structure). These are cases 4 to 6 in Figure 17.  
525 Other configurations are not considered as, in case of transition from one to two vortices, the model with two  
526 degrees of freedom fails to describe adequately the wash-out process.

527 Velocities  $u_d$  and  $\bar{u}_d$  are plotted against TKE levels inside the cavity. In particular, since each velocity  
528 describes the rate of pollutant transfer out of a specific region of the cavity (box<sub>1</sub> and box<sub>2</sub> in Figure S1 in the  
529 SI), we calculate for each one of these regions the spatial average of the TKE from PIV data. In Figure 17,  
530 the spatially averaged TKE for each region is plotted against the corresponding wash-out velocity. For each  
531 configuration (numbers 1 to 7), the blue and orange markers report the results for box<sub>1</sub> and box<sub>2</sub>, respectively.  
532 The error bars represent the uncertainty of the results associated with the two parameters  $\gamma$  and  $\beta$  of the  
533 wash-out model (see Section S1 in the SI). As expected, results show a positive correlation between TKE and  
534 the wash-out velocity. Interestingly, a clear linear relationship can be observed for  $u_d$  (blue markers), i.e. for  
535 the velocity characterizing the exchange at the roof level. The interpretation of the behaviour of  $\bar{u}_d$  (orange  
536 markers) is less straightforward. For configurations with a single main vortex (1 to 4) the internal exchange  
537 velocity slowly grows with TKE. In configurations with two counter-rotating vortices (5-7), the non-dimensional  
538 exchange velocity  $\bar{u}_d$  is larger than in single-vortex configurations. A dependence with the local TKE levels is  
539 however less easy to enlighten, also due to the non-negligible extent of the error bars, the limited number (only  
540 three) of data points available in the present analysis, and the lack of a perfect two-dimensionality of the flow  
541 in the lower cell. The existence of different trends of  $\bar{u}_d$  as a function of  $u_*$  further suggests that (differently  
542 from the case of  $u_d$ ) this exchange process may be affected by the topology of the mean flow. Enlightening this  
543 feature would require a more in-depth analysis of the transport mechanisms and further measurements in a  
544 wider range of flow conditions. In general, the measurement of the turbulent pollutant fluxes, as well as the  
545 analysis of the spatial distribution of the concentration fluctuations within the cavity, could further clarify the  
546 role of TKE in the mechanisms driving cavity ventilation and the wash-out of pollutants.

## 547 6 | CONCLUSIONS

548 We have investigated the vertical exchange of pollutants between a street canyon and the external flow. We  
549 have considered the case of a wind blowing perpendicular to the axis of the street. To grasp the physical  
550 mechanisms that govern the canyon ventilation, we have performed multiple wind tunnel experiments covering

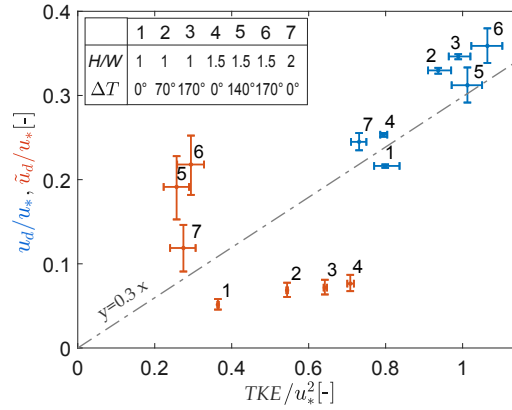


FIGURE 17 Wash-out velocity  $u_d$  (blue markers) and  $\bar{u}_d$  (orange markers) against the mean TKE in the corresponding region. Numbers 1-7 indicates the different experimental configurations. The dash-dotted line is the result of a linear regression through the origin of all the points shown in the chart.

551 a wide range of street canyon configurations. In particular, different canyon geometries and thermal conditions  
 552 at walls have been analysed.

553 In accordance with previous works, results have evidenced that the transition of the mean velocity field  
 554 within the cavity from one to two recirculating cells strongly influences the vertical removal of pollutants. The  
 555 wind tunnel experiments showed that the occurrence of this transition depends on different properties of the  
 556 street canyon.

557 As the aspect ratio of the cavity increases, the total anticlockwise vorticity fluxes at the cavity walls  
 558 increase as well. This feature induces the formation of the second counter-rotating cell, thus hindering the  
 559 canyon ventilation. As a consequence, in narrow canyons air quality at the pedestrian level is worsened.

560 Wall roughness enhances velocity gradients near the walls, inducing higher fluxes of anticlockwise vorticity.  
 561 Adding roughness to the downwind wall facilitates the transition to two recirculating cells, while roughness  
 562 elements at the upwind wall slightly influence the velocity field since the enhanced anti-clockwise vorticity is  
 563 rapidly advected outside the cavity by the mean motion.

564 Thermal fluxes at the upwind wall have negligible effects on both the mean and TKE fields. Similarly  
 565 to wall roughness, the heating of the upwind wall produces clockwise vorticity that is transferred outside the  
 566 cavity before affecting the flow.

567 From the environmental point of view, the heating of the downwind wall has opposite effects depending on  
 568 the street aspect ratio. In a square cavity, the thermal fluxes are not strong enough to modify the topology of  
 569 the mean flow streamlines, but their effect is relevant on the intensity of the TKE, which is increased in the  
 570 whole cavity. This increase in TKE seems to be associated to the acceleration of the wash-out from the canyon  
 571 to the overlying atmospheric flow, with a resulting reduction of the passive scalar concentration within the  
 572 canyon. As the aspect ratio of the cavity increases, the heating of the downwind wall has growing effects on  
 573 the velocity field. For  $H/W = 1.5$ , the heating of the wall facilitates the formation of the second cell at the  
 574 bottom of the canyon, thus slowing down the wash-out process. As a consequence, pollutants accumulate at  
 575 street level with consequent deterioration of air quality.

576 These results bring together findings from previous works which investigated the effect of single factors on

577 the velocity and concentration field inside a street canyon. The comprehensive analysis of multiple configurations  
578 involving different physical aspects (geometry, roughness, heating) displays how the different parameters interact,  
579 and traces a link between the acceleration in the wash-out process and the increase in the TKE levels, in  
580 accordance with the analysis of Salizzoni et al. [63].

581 However, further experimental studies are desirable. In particular, measurements of the turbulent and  
582 mean components of the vertical pollutant fluxes would be helpful to clarify the role of TKE in the canyon  
583 ventilation. We finally stress that the experimental results presented in this work are valid for an idealised  
584 2D street canyon with a perpendicular orientation with respect to the wind direction. However, this dataset  
585 is valuable in validating numerical simulations in two-dimensional canyons, and in reducing uncertainties in  
586 modelling the effects of the street canyon aspect ratio, wall roughness and temperature of façades on the flow  
587 and concentration field within a street.

## 588 7 | ACKNOWLEDGEMENTS

589 This study was supported by the Italian-French/French-Italian University via the Vinci Program, and by the  
590 Région Auvergne Rhône-Alpes via the SCUSI Projetc. Moreover, we would like to express our gratitude to  
591 Patrick Mejean and Nathalie Grosjean for the technical support in performing the wind tunnel experiments.

## 592 references

- 593 [1] Adrian, R., 1997. Dynamic ranges of velocity and spatial resolution of particle image velocimetry. *Measurement*  
594 *Science and Technology* 8 (12), 1393.
- 595 [2] Alexandri, E., Jones, P., 2008. Temperature decreases in an urban canyon due to green walls and green roofs in  
596 diverse climates. *Building and environment* 43 (4), 480–493.
- 597 [3] Allegrini, J., Dorer, V., Carmeliet, J., 2013. Wind tunnel measurements of buoyant flows in street canyons.  
598 *Building and Environment* 59, 315–326.
- 599 [4] Assimakopoulos, V. D., ApSimon, H., Moussiopoulos, N., 2003. A numerical study of atmospheric pollutant  
600 dispersion in different two-dimensional street canyon configurations. *Atmospheric Environment* 37 (29), 4037–  
601 4049.
- 602 [5] Baik, J.-J., Kim, J.-J., 1999. A numerical study of flow and pollutant dispersion characteristics in urban street  
603 canyons. *Journal of applied meteorology* 38 (11), 1576–1589.
- 604 [6] Banerjee, T., Katul, G., Fontan, S., Poggi, D., Kumar, M., 2013. Mean flow near edges and within cavities  
605 situated inside dense canopies. *Boundary-layer meteorology* 149 (1), 19–41.
- 606 [7] Barlow, J. F., Belcher, S. E., 2002. A wind tunnel model for quantifying fluxes in the urban boundary layer.  
607 *Boundary-Layer Meteorology* 104 (1), 131–150.
- 608 [8] Berkowicz, R., 2000. Ospm-a parameterised street pollution model. *Environmental monitoring and assessment*  
609 65 (1-2), 323–331.
- 610 [9] Bibri, S. E., Krogstie, J., 2017. Smart sustainable cities of the future: An extensive interdisciplinary literature  
611 review. *Sustainable Cities and Society* 31, 183–212.
- 612 [10] Bozovic, R., Maksimovic, C., Mijic, A., Smith, K., Suter, I., Van Reeuwijk, M., 2017. Blue green solutions. a  
613 systems approach to sustainable and cost-effective urban development.

- 614 [11] Cai, X.-M., 2012. Effects of wall heating on flow characteristics in a street canyon. *Boundary-layer meteorology*  
615 142 (3), 443–467.
- 616 [12] Carpentieri, M., Hayden, P., Robins, A. G., 2012. Wind tunnel measurements of pollutant turbulent fluxes in  
617 urban intersections. *Atmospheric Environment* 46, 669–674.
- 618 [13] Castro, I., Robins, A., 1977. The flow around a surface-mounted cube in uniform and turbulent streams. *Journal*  
619 *of fluid Mechanics* 79 (2), 307–335.
- 620 [14] Caton, F., Britter, R., Dalziel, S., 2003. Dispersion mechanisms in a street canyon. *Atmospheric Environment*  
621 37 (5), 693–702.
- 622 [15] Chang, K., Constantinescu, G., Park, S.-o., 2006. Analysis of the flow and mass transfer processes for the  
623 incompressible flow past an open cavity with a laminar and a fully turbulent incoming boundary layer. *Journal*  
624 *of Fluid Mechanics* 561, 113–145.
- 625 [16] Cui, Z., Cai, X., J Baker, C., 2004. Large-eddy simulation of turbulent flow in a street canyon. *Quarterly Journal*  
626 *of the Royal Meteorological Society* 130 (599), 1373–1394.
- 627 [17] Fackrell, J., 1980. A flame ionisation detector for measuring fluctuating concentration. *Journal of Physics E:*  
628 *Scientific Instruments* 13 (8), 888.
- 629 [18] Fellini, S., Salizzoni, P., Soulhac, L., Ridolfi, L., 2019. Propagation of toxic substances in the urban atmosphere:  
630 A complex network perspective. *Atmospheric Environment* 198, 291–301.
- 631 [19] Georgakis, C., Santamouris, M., 2006. Experimental investigation of air flow and temperature distribution in  
632 deep urban canyons for natural ventilation purposes. *Energy and buildings* 38 (4), 367–376.
- 633 [20] Gromke, C., Ruck, B., 2007. Influence of trees on the dispersion of pollutants in an urban street canyon -  
634 Experimental investigation of the flow and concentration field. *Atmospheric Environment* 41 (16), 3287–3302.
- 635 [21] Haaland, C., van den Bosch, C. K., 2015. Challenges and strategies for urban green-space planning in cities  
636 undergoing densification: A review. *Urban forestry & urban greening* 14 (4), 760–771.
- 637 [22] Harman, I., Belcher, S., 2006. The surface energy balance and boundary layer over urban street canyons. *Quarterly*  
638 *Journal of the Royal Meteorological Society* 132 (621), 2749–2768.
- 639 [23] Heilig, G. K., 2012. World urbanization prospects: the 2011 revision. United Nations, Department of Economic  
640 and Social Affairs (DESA), Population Division, Population Estimates and Projections Section, New York 14.
- 641 [24] Hertel, O., De Leeuw, F. A., Jensen, S. S., Gee, D., Herbarth, O., Pryor, S., Palmgren, F., Olsen, E., et al.,  
642 2001. Human exposure to outdoor air pollution (IUPAC technical report). *Pure and Applied Chemistry* 73 (6),  
643 933–958.
- 644 [25] Hotchkiss, R. S., 1973. Air pollution transport in street canyons. Prepared for EPA.
- 645 [26] Hunt, G., Linden, P., 1999. The fluid mechanics of natural ventilation—displacement ventilation by buoyancy-  
646 driven flows assisted by wind. *Building and Environment* 34 (6), 707–720.
- 647 [27] Hussain, M., Lee, B. E., 1980. A wind tunnel study of the mean pressure forces acting on large groups of low-rise  
648 buildings 6, 207–225.
- 649 [28] Hyun, B., Balachandar, R., Yu, K., Patel, V., 2003. Assessment of piv to measure mean velocity and turbulence  
650 in open-channel flow. *Experiments in Fluids* 35 (3), 262–267.
- 651 [29] Irwin, H., 1981. The design of spires for wind simulation. *Journal of Wind Engineering and Industrial Aerody-*  
652 *namics* 7 (3), 361 – 366.

- 653 [30] Jeong, S. J., Andrews, M. J., 2002. Application of the  $k-\epsilon$  turbulence model to the high Reynolds number  
654 skimming flow field of an urban street canyon. *Atmospheric environment* 36 (7), 1137–1145.
- 655 [31] Johnson, W., Ludwig, F., Dabberdt, W., Allen, R., 1973. An urban diffusion simulation model for carbon  
656 monoxide. *Journal of the Air Pollution Control Association* 23 (6), 490–498.
- 657 [32] Kim, J.-J., Baik, J.-J., 2001. Urban street-canyon flows with bottom heating. *Atmospheric Environment* 35 (20),  
658 3395–3404.
- 659 [33] Kovar-Panskus, A., Moulinneuf, L., Savory, E., Abdelqari, A., Sini, J.-F., Rosant, J.-M., Robins, A., Toy, N.,  
660 2002. A wind tunnel investigation of the influence of solar-induced wall-heating on the flow regime within a  
661 simulated urban street canyon. *Water, Air and Soil Pollution: Focus* 2 (5-6), 555–571.
- 662 [34] Kukkonen, J., Valkonen, E., Walden, J., Koskentalo, T., Aarnio, P., Karppinen, A., Berkowicz, R., Kartastenpää,  
663 R., 2001. A measurement campaign in a street canyon in Helsinki and comparison of results with predictions of  
664 the ospm model. *Atmospheric Environment* 35 (2), 231–243.
- 665 [35] Lee, I. Y., Park, H. M., 1994. Parameterization of the pollutant transport and dispersion in urban street canyons.  
666 28 (14), 2343–2349.
- 667 [36] Lee, S.-H., Lee, H., Park, S.-B., Woo, J.-W., Lee, D.-I., Baik, J.-J., 2016. Impacts of in-canyon vegetation  
668 and canyon aspect ratio on the thermal environment of street canyons: numerical investigation using a coupled  
669 WRF-VUCM model. *Quarterly Journal of the Royal Meteorological Society* 142 (699), 2562–2578.
- 670 [37] Leonardi, S., Orlandi, P., Antonia, R. A., 2007. Properties of d-and k-type roughness in a turbulent channel  
671 flow. *Physics of fluids* 19 (12), 125101.
- 672 [38] Li, X.-X., Britter, R., Norford, L. K., 2016. Effect of stable stratification on dispersion within urban street  
673 canyons: A large-eddy simulation. *Atmospheric environment* 144, 47–59.
- 674 [39] Li, X.-X., Britter, R. E., Norford, L. K., Koh, T.-Y., Entekhabi, D., 2012. Flow and pollutant transport in urban  
675 street canyons of different aspect ratios with ground heating: large-eddy simulation. *Boundary-layer meteorology*  
676 142 (2), 289–304.
- 677 [40] Lin, J.-C., Rockwell, D., 2001. Organized oscillations of initially turbulent flow past a cavity. *Aiaa Journal*  
678 39 (6), 1139–1151.
- 679 [41] Liu, C.-H., Barth, M. C., Leung, D. Y., 2004. Large-eddy simulation of flow and pollutant transport in street  
680 canyons of different building-height-to-street-width ratios. *Journal of Applied Meteorology* 43 (10), 1410–1424.
- 681 [42] Llaguno-Munitxa, M., Bou-Zeid, E., Hultmark, M., 2017. The influence of building geometry on street canyon  
682 air flow: Validation of large eddy simulations against wind tunnel experiments. *Journal of Wind Engineering  
683 and Industrial Aerodynamics* 165, 115–130.
- 684 [43] Louka, P., Vachon, G., Sini, J.-F., Mestayer, P., Rosant, J.-M., 2002. Thermal effects on the airflow in a street  
685 canyon - Nantes' 99 experimental results and model simulations. *Water, air and soil pollution: Focus* 2 (5-6),  
686 351–364.
- 687 [44] Marucci, D., Carpentieri, M., 2019. Effect of local and upwind stratification on flow and dispersion inside and  
688 above a bi-dimensional street canyon. *Building and Environment* 156, 74–88.
- 689 [45] Mehta, U. B., Lavan, Z., 1969. Flow in a two dimensional channel with a rectangular cavity. *Journal of Applied  
690 Mechanics* 36, 897–901.
- 691 [46] Meroney, R. N., Pavageau, M., Rafailidis, S., Schatzmann, M., 1996. Study of line source characteristics for  
692 2-d physical modelling of pollutant dispersion in street canyons. *Journal of wind Engineering and industrial  
693 Aerodynamics* 62 (1), 37–56.

- 694 [47] Mori, T., Naganuma, K., 2009. Experimental investigation of the three-dimensional nature of turbulent flow  
695 over a rectangular cavity. *Journal of Fluid Science and Technology* 4 (3), 746–757.
- 696 [48] Murena, F., Di Benedetto, A., D’Onofrio, M., Vitiello, G., 2011. Mass transfer velocity and momentum vertical  
697 exchange in simulated deep street canyons. *Boundary-layer meteorology* 140 (1), 125.
- 698 [49] Murena, F., Mele, B., 2016. Effect of balconies on air quality in deep street canyons. *Atmospheric Pollution  
699 Research* 7 (6), 1004–1012.
- 700 [50] Nakamura, Y., Oke, T. R., 1988. Wind, temperature and stability conditions in an east-west oriented urban  
701 canyon. *Atmospheric Environment* (1967) 22 (12), 2691–2700.
- 702 [51] Nazarian, N., Martilli, A., Kleissl, J., 2018. Impacts of realistic urban heating, part I: spatial variability of mean  
703 flow, turbulent exchange and pollutant dispersion. *Boundary-layer meteorology* 166 (3), 367–393.
- 704 [52] Niachou, K., Livada, I., Santamouris, M., 2008. Experimental study of temperature and airflow distribution  
705 inside an urban street canyon during hot summer weather conditions. part II: Airflow analysis. *Building and  
706 environment* 43 (8), 1393–1403.
- 707 [53] Nironi, C., 2013. Concentration fluctuations of a passive scalar in a turbulent boundary layer. Ph.D. thesis.
- 708 [54] Nironi, C., Salizzoni, P., Marro, M., Mejean, P., Grosjean, N., Soulhac, L., 2015. Dispersion of a passive scalar  
709 fluctuating plume in a turbulent boundary layer. part i: Velocity and concentration measurements. *Boundary-  
710 layer meteorology* 156 (3), 415–446.
- 711 [55] Offerle, B., Eliasson, I., Grimmond, C., Holmer, B., 2007. Surface heating in relation to air temperature, wind  
712 and turbulence in an urban street canyon. *Boundary-Layer Meteorology* 122 (2), 273–292.
- 713 [56] Oke, T. R., 1988. Street design and urban canopy layer climate. *Energy and Buildings* 11, 103–113.
- 714 [57] Oke, T. R., 2002. *Boundary layer climates*. Routledge.
- 715 [58] Olshanskii, M. A., Heister, T., Rebholz, L. G., Galvin, K. J., 2015. Natural vorticity boundary conditions on  
716 solid walls. *Computer Methods in Applied Mechanics and Engineering* 297, 18–37.
- 717 [59] Pavageau, M., Schatzmann, M., 1999. Wind tunnel measurements of concentration fluctuations in an urban  
718 street canyon. *Atmospheric Environment* 33 (24-25), 3961–3971.
- 719 [60] Prasad, A. K., 2000. Particle image velocimetry. *Current Science-Bangalore-* 79 (1), 51–60.
- 720 [61] Salizzoni, P., 2006. Mass and momentum transfer in the urban boundary layer. Ph.D. thesis, Ecully, Ecole  
721 centrale de Lyon.
- 722 [62] Salizzoni, P., Marro, M., Soulhac, L., Grosjean, N., Perkins, R. J., 2011. Turbulent transfer between street  
723 canyons and the overlying atmospheric boundary layer. *Boundary-layer meteorology* 141 (3), 393–414.
- 724 [63] Salizzoni, P., Soulhac, L., Mejean, P., 2009. Street canyon ventilation and atmospheric turbulence. *Atmospheric  
725 Environment* 43 (32), 5056–5067.
- 726 [64] Salizzoni, P., Soulhac, L., Mejean, P., Perkins, R. J., 2008. Influence of a two-scale surface roughness on a  
727 neutral turbulent boundary layer. *Boundary-layer meteorology* 127 (1), 97–110.
- 728 [65] Santamouris, M., Papanikolaou, N., Livada, I., Koronakis, I., Georgakis, C., Argiriou, A., Assimakopoulos, D.,  
729 2001. On the impact of urban climate on the energy consumption of buildings. *Solar energy* 70 (3), 201–216.
- 730 [66] Shi, L., Wang, Y., Jin, Y., Zhang, G., Zhang, D., 2019. Parametrical study and turbulence analysis of high-speed  
731 flows around an open cavity using large eddy simulation. *Fluid Dynamics Research* 51 (3), 035503.

- 732 [67] Sini, J.-F., Anquetin, S., Mestayer, P. G., 1996. Pollutant dispersion and thermal effects in urban street canyons.  
733 *Atmospheric environment* 30 (15), 2659–2677.
- 734 [68] Snyder, W., 1994. Some observations of the influence of stratification on diffusion in building wakes. In: Castro,  
735 I., Rockliff, N. (Eds.), *Stably Stratified Flows and Dispersion over Topography*. Claredon Press, pp. 301–324.
- 736 [69] Solazzo, E., Britter, R., 2007. Transfer processes in a simulated urban street canyon. *Boundary-Layer Meteorol-*  
737 *ogy* 124 (1), 43–60.
- 738 [70] Solazzo, E., Cai, X., Vardoulakis, S., 2008. Modelling wind flow and vehicle-induced turbulence in urban streets.  
739 *Atmospheric Environment* 42 (20), 4918–4931.
- 740 [71] Soulhac, L., 2000. Modélisation de la dispersion atmosphérique à l'intérieur de la canopée urbaine. Ph.D. thesis,  
741 Ecole Centrale de Lyon.
- 742 [72] Soulhac, L., Nguyen, C. V., Volta, P., Salizzoni, P., 2017. The model sirane for atmospheric urban pollutant  
743 dispersion. part iii: Validation against no2 yearly concentration measurements in a large urban agglomeration.  
744 *Atmospheric environment* 167, 377–388.
- 745 [73] Soulhac, L., Salizzoni, P., 2010. Dispersion in a street canyon for a wind direction parallel to the street axis.  
746 *Journal of Wind Engineering and Industrial Aerodynamics* 98 (12), 903–910.
- 747 [74] Soulhac, L., Salizzoni, P., Cierco, F.-X., Perkins, R., 2011. The model sirane for atmospheric urban pollutant  
748 dispersion; part i, presentation of the model. *Atmospheric environment* 45 (39), 7379–7395.
- 749 [75] Soulhac, L., Salizzoni, P., Mejean, P., Didier, D., Rios, I., 2012. The model sirane for atmospheric urban pollutant  
750 dispersion; part ii, validation of the model on a real case study. *Atmospheric environment* 49, 320–337.
- 751 [76] Theeuwes, N., Steeneveld, G., Ronda, R., Heusinkveld, B., Van Hove, L., Holtslag, A., 2014. Seasonal dependence  
752 of the urban heat island on the street canyon aspect ratio. *Quarterly Journal of the Royal Meteorological Society*  
753 140 (684), 2197–2210.
- 754 [77] Uehara, K., Murakami, S., Oikawa, S., Wakamatsu, S., 2000. Wind tunnel experiments on how thermal stratifi-  
755 cation affects flow in and above urban street canyons. *Atmospheric Environment* 34 (10), 1553–1562.
- 756 [78] WHO, 2018. Ambient (outdoor) air quality and health. [https://www.who.int/news-room/factsheets/detail/  
757 ambient-\(outdoor\)-air-qualityand-health](https://www.who.int/news-room/factsheets/detail/ambient-(outdoor)-air-qualityand-health), accessed: 2019-12-05.
- 758 [79] Xie, X., Liu, C.-H., Leung, D. Y., 2007. Impact of building façades and ground heating on wind flow and  
759 pollutant transport in street canyons. *Atmospheric Environment* 41 (39), 9030–9049.
- 760 [80] Yamartino, R. J., Wiegand, G., 1986. Development and evaluation of simple models for the flow, turbulence  
761 and pollutant concentration fields within an urban street canyon. *Atmospheric Environment* (1967) 20 (11),  
762 2137–2156.